REVIEW

Computational Characterization of Nanosystems†

Xiongzhi Zeng, Wei Hu, Xiao Zheng, Jin Zhao, Zhenyu Li*, Jinlong Yang*

Hefei National Laboratory for Physical Sciences at the Microscale, University of Science and Technology of China, Hefei 230026, China

(Dated: Received on November15, 2021; Accepted on January 19, 2022)

Nanosystems play an important role in many applications. Due to their complexity, it is challenging to accurately characterize their structure and properties. An important means to reach such a goal is computational simulation, which is grounded on *ab initio* electronic structure calculations. Low scaling and accurate electronic-structure algorithms have been developed in recent years. Especially, the efficiency of hybrid density functional calculations for periodic systems has been significantly improved. With electronic structure information, simulation methods can be developed to directly obtain experimentally comparable data. For example, scanning tunneling microscopy images can be effectively simulated with advanced algorithms. When the system we are interested in is strongly coupled to environment, such as the Kondo effect, solving the hierarchical equations of motion turns out to be an effective way of computational characterization. Furthermore, the first principles simulation on the excited state dynamics rapidly emerges in recent years, and nonadiabatic molecular dynamics method plays an important role. For nanosystem involved chemical processes, such as graphene growth, multiscale simulation methods should be developed to characterize their atomic details. In this review, we review some recent progresses in methodology development for computational characterization of nanosystems. Advanced algorithms and software are essential for us to better understand of the nanoworld.

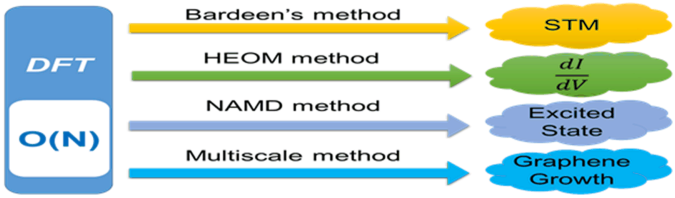

Key words: Density functional theory, Linear-scaling algorithms, Open system, Nonadiabatic molecular dynamics, Multiscale methods

I. INTRODUCTION

Nanosystems have attracted broad research interest in last decades. Due to their complexity in structure and interaction, it is challenging to accurately characterize nanosystems, where a combination of experimental and theoretical efforts is considered to be important. Phenomenological models can be used to explain experiments, however, with limit prediction power. Computational simulation which is also called "numerical experiment" sets up a more concrete bridge between experiment and theory. To effectively simulate nanosystems, efficient and accurate simulation methods should be developed.

Computational simulation is grounded on *ab initio* electronic structure calculations, which can be performed using quantum-chemical approaches (including the Hartree-Fock theory and post-Hartree-Fock methods) [1] or density functional theory (DFT) [2]. The former can produce accurate results with the price of high computational costs. The latter is computational-

†Part of Special Issue "In Memory of Prof. Nanquan Lou on the occasion of his 100th anniversary".

*Authors to whom correspondence should be addressed. E-mail: zyli@ustc.edu.cn, jlyang@ustc.edu.cn

 ©2022 Chinese Physical Society

ly more efficient, and its accuracy depends on the approximation of exchange-correlation functional [3]. Conventional DFT has a $O(N^3)$ scaling to the number of atoms N, although it is more favorable compared to accurate quantum chemical methods, which still makes it difficult to be applied to large systems. If hybrid functional, which can improve the prediction accuracy for some properties [4−7], is used, the computational scaling increases to $O(N^4)$ due to the evaluation of the Hartree-Fock exchange matrix elements. Lower scaling DFT methods are essential for simulating complex nanosystems. Recently, important progresses have been achieved in this direction.

With electronic structure information, it is important for theoretical simulations to be of the ability to predict something which can be directly compared to experimental results. Various spectroscopic techniques are used in experiments to probe the properties of local bonding and chemical structures. Density-functional perturbation theory [8] is a powerful theoretical technique to simulate experimental vibrational spectra, such as infrared and Raman spectrum. Scanning tunneling microscopy (STM) has been widely used to characterize adsorbates on surface [9−13], which usually can be simulated within the Tersoff-Hamann approximation [14, 15]. When a chemically modified STM tip [16, 17] is used, new phenomenon such as negative differential resistance [18, 19] can be observed. Then, the Bardeen's approach [20] with the STM tip explicitly considered should be used.

When the system is strongly correlated and coupled with environment, such as with the Kondo effect [11] and Coulomb blockade [21], the simulation becomes more challenging [22]. Various methods have been proposed for such systems [23−28], of which the Hierarchical Equations of Motion (HEOM) in the framework of quantum dissipation theory is a promising one, where the system is treated with high level quantum dynamics approaches, while the surrounding environment is described by quantum statistical means [29−34]. The HEOM method is rigorous in considering the combined effects of strong e-e interaction, impurity-environment dissipative coupling and non-Markovian memory.

The optical properties of nanosystems are usually related to the excited state properties, where the conventional DFT fails [35, 36]. Quasi-particle energies and optical spectra can be investigated by employing many-body Green's function approach based on the GW approximation and Bethe-Salpeter equation (GW+BSE) [37]. Alternatively, linear response time-dependent DFT can also be used to study excited state properties [38]. Furthermore, the optical excitation often drives ultrafast excited carrier dynamics. In this case, different interactions, such as electron-phonon interaction, spin-orbital coupling and the many-body effects of electron-hole pair come into playing collectively. To understand such complex excited carrier dynamics, nonadiabatic molecular dynamics (NAMD) methods has been rapidly developed in recent 20 years, which can provide the atomic-scale picture [39−43]. The classical path approximation (CPA) [44] combined with different surface hopping approaches such as Tully's fewest switches surface hopping [45] has been used to reduce the computation cost of NAMD simulations [39, 46]. Very recently, NAMD based on GW plus real-time BSE method has been developed, in which the many-body effect of electron-hole is included explicitly for exciton dynamics [47].

To effectively simulate systems with many elementary reactions with complex external environment involved, multiscale methods should be used. For example, various simulation techniques, such as molecular dynamics (MD) [48, 49], kinetic Monte Carlo (kMC) [50−52], rate equations [50, 53], phase field [54], and computational fluid dynamics [55], have been used to study graphene growth. Brute force MD simulations can only explore a very limited time scale. Solving rate equations in principle has no time limitation but it is based on a homogeneous assumption. As a time scale coarse graining technique, kMC can simulate inhomogeneous systems at a large time scale. Some system-specific algorithms, such as floating simulation box [52], time scale separation [51], and mean field approximation for specific species [51], can be used to speed up kMC simulations [56−59].

In this review, we review some recent progresses in methods development for computational characterization of nanosystems. Various techniques are proposed to accelerate electronic structure calculations, which have been implemented in Hefei Order-N Package for Ab-initio Simulations (HONPAS). Highly efficient method for STM image simulation based on the Bardeen's formulism is reported. The Kondo effect and related quantum phenomena can be simulated with the program named HEOM for QUantum Impurity with a Correlated Kernel (HEOM-QUICK). Properties of ex-

DOI:10.1063/1674-0068/cjcp2111233 ©2022 Chinese Physical Society

cited states such as the ultrafast dynamics of photoexcited charge carriers can be simulated via the *ab initio* nonadiabatic molecular dynamics software, Hefei-NAMD. Multiscale methods are developed to study the complex graphene growth process. Advanced algorithms and software packages can help us to deepen our understanding of the nanoworld.

II. LINEAR-SCALING ELECTRONIC STRUCTURE CALCULATIONS

In DFT [60], we numerically solve the Kohn-Sham (KS) equation

$$\left(\hat{t}_{\mathrm{s}}+\upsilon_{\mathrm{H}}+\upsilon_{\mathrm{xc}}+\upsilon_{\mathrm{ext}}\right)\psi_i=\varepsilon_i\psi_i\left(r\right) \tag{1}$$

where ψ_i is a KS orbital with an energy ε_i. The exact form of the exchange-correlation potential υ_{xc} in the effective Hamiltonian is unknown. In practical calculations, different approximate exchange-correlation energy functionals are adopted. The KS orbital ψ_i can be written as a linear combination of atomic orbitals:

$$\psi_i\left(r\right)=\sum_{\mu}^{N_b}c_{\mu i}\phi_\mu\left(r\right) \tag{2}$$

Then, the density matrix can be obtained from coefficients of occupied KS orbitals $\rho_{\mu\nu}=\sum_{i}^{\mathrm{occ}}c_{\mu i}c_{\nu i}$. The computational scaling is $\mathrm{O}(N^3)$ where N is the number of atoms [61].

In computational characterization of nanosystems, it is frequently required to simulate thousands of atoms. It is thus desirable to have linear scaling electronic-structure algorithms [61, 62]. The Kohn's nearsightedness principle [63], which states that the local properties of a quantum system do not see an external-potential change from a far-away distance, plays an important role in many linear scaling algorithms. From this point of view, strictly localized orbitals such as numerical atomic orbitals (NAOs) are more suitable for linear-scaling calculations, compared to the commonly used Gaussian orbitals with a long tail. Therefore, NAOs are widely used in packages such as SIESTA [64], DMOL [65], OPENMX [66], and HONPAS [67] to construct a sparse Hamiltonian.

Linear scaling algorithms can be constructed based on the density matrix, such as the divide-and-conquer [68], density matrix minimization [69], the second-order trace-correcting density matrix purification algorithm [70−72]. In the second-order trace-correcting density matrix purification algorithm, the following iteration of density matrix is used for spin-restricted systems,

$$\rho_{n+1}\left(\rho_n\right)=\begin{cases}\rho_n^2, & \mathrm{Tr}\left(\rho_n\right)\geq N_e/2\\ 2\rho_n-\rho_n^2, & \mathrm{Tr}\left(\rho_n\right)<N_e/2\end{cases} \tag{3}$$

Its spin-unrestricted version can be realized by determining the correct electron occupations of different spin channels from the Aufbau principle [73]. Band edge states [74], maximally localized Wannier functions [75], optical dielectric constant and Born effective charge [76] can also be calculated with a linear scaling approach based on the second-order trace-correcting density matrix purification algorithm.

In DFT electronic structure calculations, local density approximation [77] and generalized gradient approximation [78] are widely used to construct exchange-correlation energy functional. Unfortunately, they are not accurate enough to describe band gap [79]. Hybrid exchange-correlation functionals [4, 6, 7] are typically more accurate since they include a fraction of the non-local Hartree-Fock type exchange (HFX) contribution. The HFX can be expressed as:

$$\upsilon_{\mathrm{HFX}}\left(r,r'\right)\psi_i\left(r'\right)=-\sum_{j}^{N_{\mathrm{occ}}}\psi_j\left(r\right)\int\frac{\psi_j\left(r'\right)\psi_i\left(r'\right)}{\left|r-r'\right|}\mathrm{d}r' \tag{4}$$

The HFX energy is

$$E_{\mathrm{HFX}}=-\sum_{ij}^{N_{\mathrm{occ}}}\iint\frac{\psi_i\left(r\right)\psi_j\left(r'\right)\psi_j\left(r\right)\psi_i\left(r'\right)}{\left|r-r'\right|}\mathrm{d}r\mathrm{d}r'=-\sum_{\mu\nu\lambda\sigma}^{N_{\mathrm{b}}}\rho_{\mu\lambda}\rho_{\nu\sigma}\iint\frac{\phi_\mu\left(r\right)\phi_\nu\left(r'\right)\phi_\lambda\left(r\right)\phi_\sigma\left(r'\right)}{\left|r-r'\right|}\mathrm{d}r\mathrm{d}r' \tag{5}$$

The two-electron four-center $(\mu\nu\lambda\sigma)$ integration or the so-called electron repulsion integrals (ERIs) in Eq.(5)

DOI:10.1063/1674-0068/cjcp2111233 ©2022 Chinese Physical Society

is the computational bottleneck in hybrid density-functional calculations, which increases the computational scaling to $O(N^4)$. Storing and retrieving ERIs are also expensive.

Strict locality of the NAOs basis set can in principle realize linear scaling calculation of the ERIs, but with a large prefactor [80]. Using the widely used Gaussian-type orbital (GTO) basis set, ERIs can be calculated analytically [81−83]. However, the calculation will not be stable with a simple truncation due to the long tail of the Gaussian function. A hybrid algorithm was developed, denoted as NAO2GTO [84], which takes advantages of both GTO and NAO by fitting NAOs with GTOs. As a result, there is a significant reduction of the prefactor for computation of HFX, and a noticeable increase in computation speed especially when combined with dynamic parallel schemes [85, 86]. As shown in FIG. 1, an almost ideal parallelization scaling is achieved for ERI calculations of two model systems, a 2000 Si atom unit cell with single-ζ plus polarization basis set and a 512 Si atom unit cell with double-ζ plus polarization basis set. All these NAO based linear-scaling algorithms described above have been implemented in HONPAS.

When a large basis set, such as plane waves, is used in solid systems, it is computationally expensive to calculate HFX. The low-rank approximations [87, 88] of adaptively compressed exchange operator [89] and interpolative separable density fitting [90] algorithms significantly reduce the computational cost and memory usage of hybrid functional calculations within the plane-wave basis set. By finding a smaller set of linearly independent basis to represent the orbital-pair products, the number of Poisson-like equations to be solved can be significantly reduced, such as in interpolative separable density fitting decomposition [90]

$$\psi_\mu(\boldsymbol{r})\,\psi_\nu(\boldsymbol{r}) \approx \sum_{i=1}^{N_i} \zeta_i(\boldsymbol{r})\,\psi_\mu(\boldsymbol{r}_i)\,\psi_\nu(\boldsymbol{r}_i) \tag{6}$$

where the interpolation points $\{\boldsymbol{r}_i\}_{i=1}^{N_i}$ is a small subset of the real-space integration grid points $\{\boldsymbol{r}_g\}_{g=1}^{N_g}$. When incorporating with the adaptively compressed exchange operator [89], the adaptively compressed exchange operator combined with the interpolative separable density fitting method only requires to update the exchange operator with significantly reduced cost [91, 92]. The decomposition of a matrix into an orthogonal matrix and a triangular matrix (QR decomposition) with column pivoting step has been found to be the expensive step for large-scale plane-wave-based hybrid functional calculations. Several algorithms were proposed to further improve the efficiency of calculation. The centroidal Voronoi tessellation procedure computed with machine learning K-Means clustering algorithm is powerful and efficient to gather desired interpolation points [93, 94]. Similar techniques can also be used to speed up linear response time-dependent DFT [95] and GW [96] calculations.

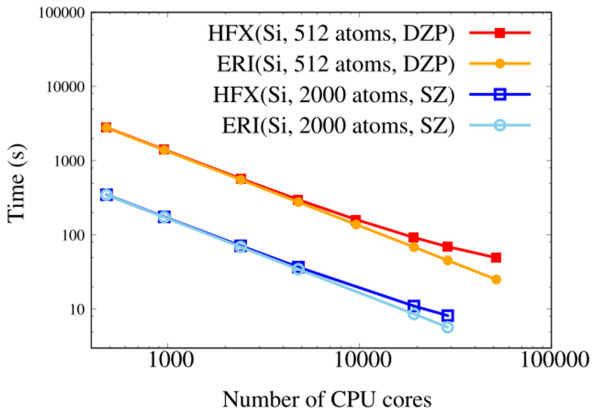

FIG. 1 Scalability for bulk silicon with different system sizes and basis sets. Adapted from Ref.[86]. Copyright 2020 Elsevier.

III. METHODS FOR NANOSYSTEM CHARACTERIZATION

With electronic structure obtained, many properties of a nanosystem can be calculated and some of them can be directly compared to experimental observations, which provides a reliable way to characterize nanosystems. For some nanosystems, such as strongly correlated systems, system with nonadiabatic coupling to excited states, or systems in a complex reaction network, specific techniques should be developed to simulate them.

A. Atomic structure

To characterize a nanosystem, the most fundamental information which should be obtained is its atomic structure. A widely used experimental means to characterize atomic structure is STM [97−99]. However, it should be emphasized that, just like other instruments, an STM does not really see atoms. What we can obtain

DOI:10.1063/1674-0068/cjcp2111233 ©2022 Chinese Physical Society

from STM is some tunneling current data. Interpreting these data to obtain atomic structure information typically relies on computational simulations of STM images. Therefore, STM image simulation represents a good example to demonstrate computational characterization of nanosystems.

By comparing simulated and experimentally observed STM images, the most reasonable structure model can be obtained. There are different models [100−104] to calculate the tunneling current for STM image simulation, of which the well-known Bardeen formulism [20] gives the current as

$$I = \frac{2\pi e}{\hbar} \sum_{\mathrm{t,s}} \left[f\left(\varepsilon_{\mathrm{t}}\right) - f\left(\varepsilon_{\mathrm{s}}\right) \right] \left| M_{\mathrm{ts}} \right|^2 \delta\left(\varepsilon_{\mathrm{t}} - \varepsilon_{\mathrm{s}} + eV\right) \quad (7)$$

where $f\left(\varepsilon_{\mathrm{s}}\right)$ is the electron distribution function, and t and s represent tip and sample, respectively. V is the applied voltage and M_{ts} is the tunneling matrix elements between the tip and sample states.

$$M_{\mathrm{ts}} = -\frac{1}{2} \int_{\Sigma} \left[\psi_{\mathrm{t}}^{*}\left(r - r_{\mathrm{t}}\right) \nabla \varphi_{\mathrm{s}}\left(r - r_{\mathrm{s}}\right) - \varphi_{\mathrm{s}}\left(r - r_{\mathrm{s}}\right) \nabla \psi_{\mathrm{t}}^{*}\left(r - r_{\mathrm{t}}\right) \right] \mathrm{d}S \quad (8)$$

where Σ is a dividing surface between the tip and the sample.

A simplification of the Bardeen's theory is proposed by the Tersoff and Hamann [14, 15]. When the tip's wavefunction is simple enough, the tunneling current is directly related to the local density of states of the sample around the Fermi energy

$$I \propto \int_{\varepsilon_{\mathrm{F}}}^{\varepsilon_{\mathrm{F}}+\mathrm{eV}} \rho_s\left(\vec{r}, \varepsilon\right) \mathrm{d}E \quad (9)$$

$$\rho_s\left(\vec{r}, \varepsilon\right) = \sum_{\mu} \left|\psi_{\mu}\left(\vec{r}\right)\right|^2 \delta\left(\varepsilon - \varepsilon_{\mu}\right) \quad (10)$$

Such a simple model has been successfully used to identify molecule adsorption orientation [105, 106], analyze the electronic structure and magnetic behaviors [11], and evaluate the interactions between the substrate and molecular sample [107−110].

When the tip structure is complex especially when it is chemically modified, the assumption adopted in the Tersoff-Hamann model becomes unacceptable. Then, the Bardeen's approach should be used, which requires to calculate the tunneling matrix elements as in Eq.(8).

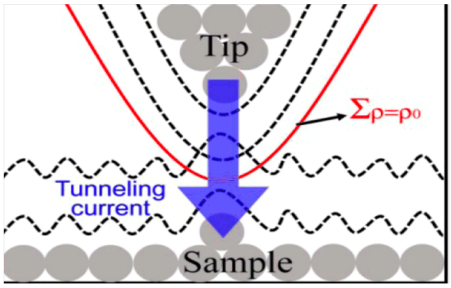

FIG. 2 A schematic view of the tip wave functions and the sample wave functions having overlap in the vacuum region. A specific surface with constant electron density enveloping the tip. Adapted from Ref.[112]. Copyright 2014 American Chemical Society.

By incorporating tip wave functions, it is possible to predict the tip structure in STM experiment [111]. A surface enveloping the tip with a constant electron density (FIG. 2) can be selected as the separate surface Σ. The equation of this surface can be written as $h_{\Sigma}=\log\left(\frac{\rho_t\left(\vec{r}\right)}{\rho_0}\right)=0$. With the relative coordinates $\overrightarrow{r_0}$ between the tip and sample, the tunneling matrix elements can be reformulated in a convolution form

$$M_{\mathrm{ts}}=-\frac{\hbar}{2m} \int \vec{v}\left(\vec{r}-\vec{r_0}\right) \nabla \varphi_{\mathrm{s}}\left(\vec{r}\right) - \varphi_{\mathrm{s}}\left(\vec{r}\right) u\left(\vec{r}-\vec{r_0}\right) \mathrm{d}r^3 \quad (11)$$

where

$$u\left(\vec{r}-\vec{r_0}\right) = \nabla \psi_{\mathrm{t}}^{*}\left(\vec{r}-\vec{r}_0\right) \vec{n}_{\mathrm{t}}\left(\vec{r}-\vec{r}_0\right) \delta[h\left(\vec{r}-\vec{r}_0\right)] \quad (12)$$

$$\tilde{\nu}\left(\vec{r}-\vec{r_0}\right) = \psi_{\mathrm{t}}^{*}\left(\vec{r}-\vec{r}_0\right) \vec{n}_{\mathrm{t}}\left(\vec{r}-\vec{r}_0\right) \delta\left[h\left(\vec{r}-\vec{r}_0\right)\right] \quad (13)$$

with the unit normal vector of surfacen $\vec{n}_{\mathrm{t}}\left(\vec{r}-\vec{r}_0\right)= \nabla\rho_{\mathrm{t}}\left(\vec{r}\right) / \left|\nabla\rho_{\mathrm{t}}\left(\vec{r}\right)\right|$. The delta function of h is constructed as a constraint to make the integration done on surface Σ. To speed up the simulation, a fast algorithm was proposed by calculating the integral with fast Fourier transform [112]. With the calculated M_{ts}, the STM image and I-V spectra can be easily obtained. With the new algorithm, STM images for CO adsorbed on Cu(111) surface with a tungsten tip and a CO-terminated tip can be simulated (FIG. 3). The simulated results are in good agreement with the experiment.

B. Strongly-correlated electronic state

In a strongly correlated system with localized electrons, interesting phenomenon such as the Kondo effect

DOI:10.1063/1674-0068/cjcp2111233 ©2022 Chinese Physical Society

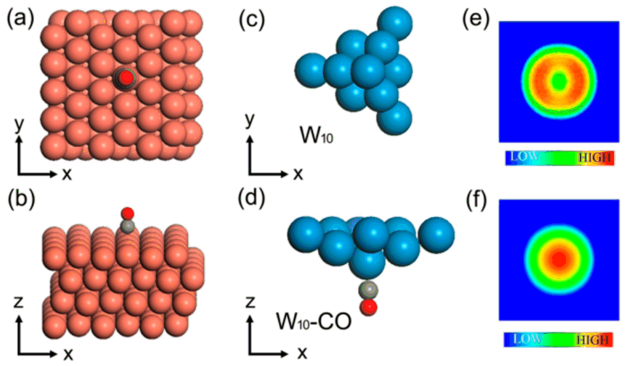

FIG. 3 Schematic (a) top and (b) side views of the CO molecule chemisorbed on the Cu(111) surface. The dull-red, gray, and red balls represent copper, carbon, and oxygen atoms, respectively. (c) Top view of the W(111) bcc pyramid tip. (d) Side view of CO adsorbed W_{10} tip. The blue, gray, and red balls represent tungsten, carbon, and oxygen atoms, respectively. Simulated STM image with (e) W_{10} or (f) W_{10}-CO tip and a sample bias of 1.0 V. Adapted from Ref.[112]. Copyright 2014 American Chemical Society.

can be observed. In nanoscience, an important type of strongly correlated system is a quantum impurity typically containing a magnetic molecule with d or f electrons. Accurate characterization of such a system from first principles is challenging, considering the intricate electron-electron and electron-environment interactions in addition to the response properties under possible external fields [22].

The HEOM method based on quantum dissipation theory has been proven to be a powerful method to theoretical simulation of the quantum impurity systems [29, 113−116]. In the framework of quantum dissipation theory, the quantum impurity is regarded as an open system that can exchange energy and particle with the surrounding environment. The total Hamiltonian of the system which models a molecule with an embedded magnetic atom (the impurity) adsorbed on a metal substrate surface under the STM tip (the reservoir environments) can be written in the Anderson impurity model [117].

$$H_{\rm T} = H_{\rm imp} + H_{\rm env} + H_{\rm coup} \tag{14}$$

where the Hamiltonian of the impurity is

$$H_{\rm imp} = \sum_{i,\sigma} \varepsilon_{i\sigma}\hat{n}_{i\sigma} + \sum_{i} U_i \hat{n}_{i\uparrow}\hat{n}_{i\downarrow} + \sum_{i<j}\sum_{\sigma} U_{ij}^{'}\hat{n}_{i\sigma}\hat{n}_{j\sigma} \tag{15}$$

Here, $\hat{n}_{i\sigma}=\hat{d}_{i\sigma}^{+}d_{i\sigma}$ is the particle number operator and $\hat{d}_{i\sigma}^{+}$ ($d_{i\sigma}$) is the creation (annihilation) operator for a spin-σ ($\sigma=\uparrow$ or $\downarrow$) electron on the ith impurity orbital of energy $\varepsilon_{i\sigma}$, and the U_i and $U_{ij}^{'}$ represent the intra- and inter-orbital Coulomb interaction strengths. The environment term with contributions from substrate and STM tip can be described at a mean-field level as

$$H_{\rm env} = \sum_{\alpha={\rm s,t}}\sum_{\sigma} \varepsilon_{\alpha\nu}\hat{c}_{\alpha\nu\sigma}^{+}\hat{c}_{\alpha\nu\sigma} \tag{16}$$

where $\hat{c}_{\alpha\nu\sigma}^{+}$ ($\hat{c}_{\alpha\nu\sigma}$) is the creation (annihilation) operator for a spin-σ electron on the single-electron state ν of energy $\varepsilon_{\alpha\nu}$. The coupling Hamiltonian is

$$H_{\rm coup} = \sum_{\alpha\nu i}\sum_{\sigma} t_{\alpha\nu i}\hat{c}_{\alpha\nu\sigma}^{+}\hat{d}_{i\sigma} + {\rm h.c.} \tag{17}$$

where $t_{\alpha\nu i}$ is the coupling strength between the impurity orbital and the electron state in the environment.

With the model defined above, what we are interested is the reduced density matrix of the impurity system $\rho^0({\rm t})={\rm tr}_{\rm env}[\rho_T(t)]$. Feynman-Vernon influence functional path-integral theory can be used to describe the dissipation of the system due to the environment [117]. By taking the time derivatives of the influence functional in a hierarchical manner, which is enabled by expanding the reservoir correlation functions by a series of exponential functions, a formally rigorous HEOM formalism can be constructed [29, 30, 118]

$$\dot{\rho}_{{\rm j}_1,\ldots j_n}^{(n)} = \left(-i\mathcal{L} + \sum_{r=1}^{n}\gamma_{j_r}\right)\rho_{j_1\ldots j_n}^{(n)} + i\sum_{j}\mathcal{A}_j\rho_{j_1\ldots j_n j}^{(n+1)} + i\sum_{r=1}^{n}\mathcal{C}_{j_r}\rho_{j_1\ldots j_{r-1}j_{r+1}\ldots j_n}^{(n-1)} \tag{18}$$

The electron-electron interaction is casted into the Liouvillian of impurity $\mathcal{L}\cdot\equiv[H_{\rm imp},\cdot]$. $\mathcal{A}_j$ and $\mathcal{C}_{j_r}$ are Grassmann superoperators defined via their actions on a system-related operator. j is a multi-component index. γ_{j_r} is the damping parameter in the exponential expansion of reservoir correlation function. $\rho^{(0)}$ is the reduced density matrix and $\{\rho_{j_1\ldots j_n}^{(n)};n{=}1,\ \ldots\ L\}$ are auxiliary density operators (ADOs) where L is the terminal or truncated tier level. The ADOs are constructed via defining reduced Liouville-space propagator at different tiers. The structure of density matrices in the HEOM method is shown in FIG. 4. Such a hierarchical structure is very useful in providing a con-

DOI:10.1063/1674-0068/cjcp2111233 ©2022 Chinese Physical Society

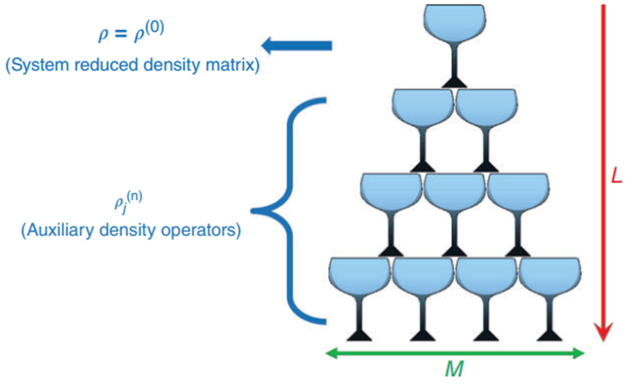

FIG. 4 Schematic diagram for the structure of HEOM. The structure of the hierarchy is characterized by the parameters M in the horizontal direction and L in the vertical direction, respectively. Here, M is the number of the exponential functions to expand the reservoir correlation functions, and L denotes the truncation tier, which is determined by the e-e interaction strength. Adapted from Ref.[22]. Copyright 2016 Wiley.

venient way to calculate reduced density matrix. Any single-electron property of a noninteracting open system can be exactly evaluated with the truncation tier being set to 2. The HEOM protocol described above has been implemented in the HEOM-QUICK package [22]. Stationary solution and expectation values of local quantum observables can be evaluated. In addition, time-evolution simulations for response properties can be obtained based on the HEOM-space linear response theory on top of the resulting stationary reduced density matrix and ADOs [119, 120].

With high-tier ADOs introduced, HEOM is difficult to be solved with a high computational cost. A number of algorithms and techniques are proposed to solve this problem. Using Matsubara spectrum decomposition or Padé spectrum decomposition to the Fermi/Bose function is an effective way to speed up calculations [29, 121, 122]. However, these methods will cost a lot of basis functions to fit the environmental correlation function near low temperature, and result in consuming a lot of memory. An efficient low-frequency logarithmic discretization scheme is proposed for the investigation of quantum impurity systems, which requires a much smaller number of exponential functions [123]. Fano spectrum decomposition scheme practically overcomes the discontinuity of Fermi and Bose functions near zero temperature, and speeds up the convergence compared to the state-of-the-art Padé spectrum decomposition [31, 32]. It is also possible to use the symmetry relation and sparsity feature of ADOs to reduce memory requirement [124]. The contribution of higher-tier ADOs can be included through a new truncation scheme [119], instead of setting all the ADOs beyond Lth tier to zero.

With these algorithms and techniques implemented, HEOM-QUICK is a powerful tool for accurate theoretical investigation of quantum impurity systems. Electronic structure information required in the Hamiltonian can be obtained from DFT or high-level quantum chemical calculations [30]. By combining DFT and the HEOM approach, experimental observations can be accurately reproduced which gives deep insights in understanding and designing nano-sized or single-molecular devices with unique electronic or magnetic properties [125−127]. In a recent example, DFT+HEOM method has been applied to simulate a surface adsorption system [128]. Co phthalocyanine can be dragged by STM tip to capture isolated Co atoms on the Au(111) surface, leading to a series of atom-molecular mold structures. Simulated differential conductance spectra and Kondo temperature agree well with the experiment (FIG. 5), which confirms the mechanism to efficiently regularize the Kondo states at atom/metal interfaces.

C. Electron and exciton dynamics

Characterization of excited state involved processes is essential in photonic device applications and design of the solar energy conversion materials [129−132]. For example, the lifetime of the excited carriers, the relaxation of the hot carriers and the charge transfer efficiency at the interface affect the efficiency of photovoltaic and photocatalytic systems collectively. For photonic devices, photoexcited carrier dynamics is linked to several different figures of merit. For instance, suppressing nonradiative electron-hole recombination and extending the carrier lifetime are required for light emitting devices. In contrast, short lifetime of excited carrier and a fast response are desirable for optical switches.

To understand the excited carrier dynamics, *ab initio* NAMD method has been developed. To describe a non-adiabatic process, we should go beyond the Born-Oppenheimer approximation. The usual way to proceed is via a so-called mixed quantum-classical approach [133] where only electrons are treated quantum mechanically and nuclei are treated classically. The quantum-backreaction problem [134] in the quantum-classical self-consistency process can be treated by the mean-field method or surface hopping method. The mean-field

DOI:10.1063/1674-0068/cjcp2111233 ©2022 Chinese Physical Society

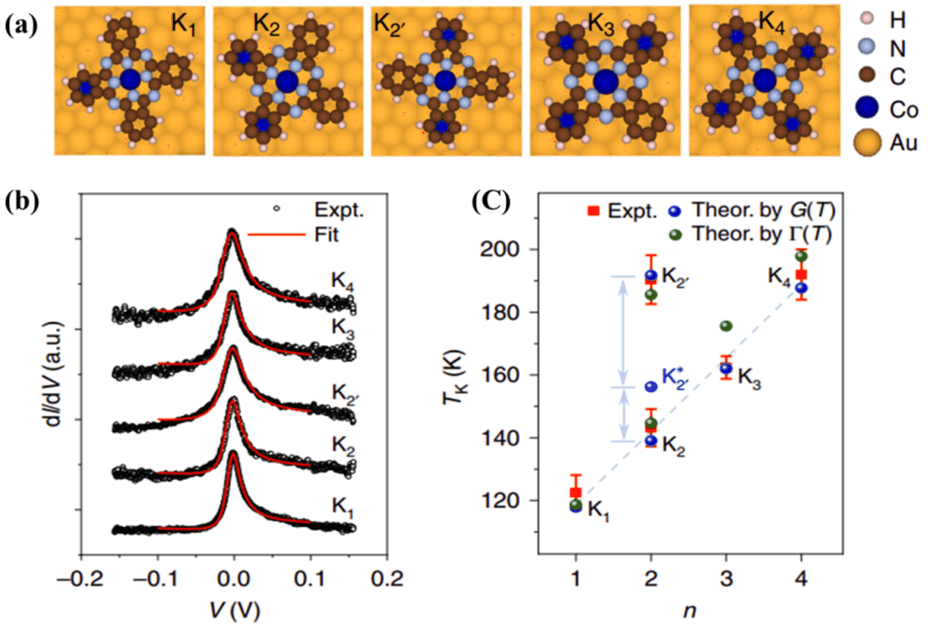

FIG. 5 (a) Structural models for the K_n complexes, where each captured Co adatom is located underneath the six-member ring of an isoindole unit. (b) Measured dI/dV spectra of the K_n complexes (n=1, 2, 2′, 3, 4). The red lines are fits of the measured data to the Fano function, and they have been shifted vertically for clarity. (c) T_K of the K_n complexes extracted from experimentally measured and theoretically calculated dI/dV spectra. Adapted from Ref.[128]. Copyright 2020 Springer Nature.

method can provide a good description of the excited state transition if the systems have similar quantum states involved in the dynamics process [133]. Surface hopping methods, such as Tully's fewest switches surface hopping algorithm [45], introduce stochastic hops between different potential energy surfaces to deal with the quantum and classical subsystem correlation.

The *ab initio* non-adiabatic simulation can start from solving the time-dependent Kohn-Sham (TDKS) equation [135]

$$i\hbar\frac{\partial}{\partial t}c_j(t) = \sum_j c_k(t)\left(\varepsilon_k\delta_{jk} - i\hbar d_{jk}(t)\right) \quad (19)$$

$$\psi_e(r,t) = \sum_j c_j(t)\,\phi_j(r,R(t)) \quad (20)$$

where orbital ψ_e is expanded in the basis of instantaneous adiabatic KS orbitals $\phi_{j/k}$, $c_j(t)$ is the time-dependent expansion coefficients. ε_k is an eigenvalue of the adiabatic KS equation. $d_{jk}(t)$ is the non-adiabatic coupling matrix elements which determine crucially the dynamics of the electron hole recombination induced by the non-adiabatic mechanism.

$$d_{jk}(t) = \langle\phi_j|\frac{\partial}{\partial t}|\phi_k\rangle = \sum_I \frac{\langle\phi_j|\nabla_{R_I}H|\phi_k\rangle}{\varepsilon_k-\varepsilon_j}\dot{R}_I \quad (21)$$

With some important ingredients prepared such as the energy difference terms $\varepsilon_k-\varepsilon_j$, the electron-phonon coupling matrix elements $\langle\phi_j|\nabla_{R_I}H|\phi_k\rangle$ and the nuclear velocity term $\dot{R}_I$, the non-adiabatic coupling matrix elements can be obtained directly in a finite difference method based on the above equation. In the fewest switches surface hopping method, the hopping probabilities between the different adiabatic KS states can be obtained from the expansion coefficients and the non-adiabatic coupling matrix elements [45].

With the non-adiabatic simulation procedure, the real-space density of excited carrier can be calculated as the norm-square of the time-dependent KS orbitals. Its time variation can be obtained as

$$\frac{d\rho(r,t)}{dt} = \sum_j\left(\frac{d}{dt}c_t^*(t)\,c_j(t)\right)\phi_j^*(r,R(t))\,\phi_j(r,R(t)) + c_j^*(t)\,c_j(t)\left(\frac{d}{dt}\phi_j^*(r,R(t))\,\phi_j(r,R(t))\right) \quad (22)$$

DOI:10.1063/1674-0068/cjcp2111233 ©2022 Chinese Physical Society

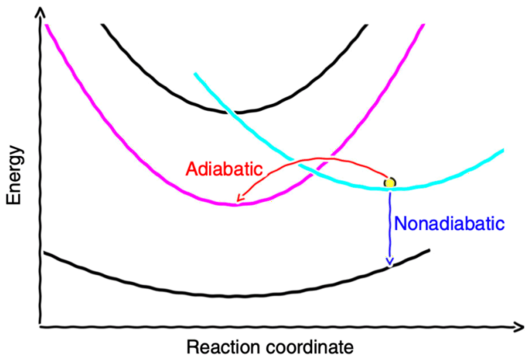

FIG. 6 Schematics of the adiabatic (red solid line) and nonadiabatic (blue solid line) charge transfer process. The solid black lines represent the potential energy surface. Adapted with permission from Ref.[39]. Copyright 2019 Wiley.

There are mainly two contributions: the NA contribution is a change primarily due to the variation of the KS states populations $c_j^*(t)\,c_j(t)$ as indicated by blue line in FIG. 6, the adiabatic contribution is from the change of the adiabatic KS orbitals $\phi_j^*(r,R(t))\,\phi_j(r,R(t))$ as indicated by red line in FIG. 6. We can obtain the various detailed dynamics information from the time variation of the real-space quantities.

In practical simulations, the classical path approximation (CPA) is frequently adopted to reduce computational costs of first principles electronic structure calculations. The basic assumption of CPA is that nuclear dynamics of the system remains unaffected by the motions of the electronic degrees of freedom. Therefore, a ground-state MD simulation can be performed first, which gives the Hamiltonian for NAMD simulations [40]. A time-dependent *ab initio* NAMD code (Hefei-NAMD) within the surface hopping-CPA framework has been recently developed [39]. It has been used to investigate the nonradiative excited carrier dynamics in different condensed matter systems including the interfacial charge transfer dynamics [135−138], the electron hole recombination dynamics [139−141] and the excited spin-polarized hole dynamics [142]. In these different dynamical simulations, it has been found the phonon excitation and e-p coupling strongly affected the excited carrier dynamics process. This method can be extended by including the nuclear quantum effects, the spin-orbit coupling, and the exciton effects.

Recently, the one-body TDKS-NAMD has been extended to many-body GW plus real-time propagation of BSE (GW+rtBSE-NAMD) for the investigation of exciton dynamics [47]. The BSE Hamiltonian used for the real-time propagation is expressed by spinor notation as:

$$\begin{aligned}\langle kcv|H|k'c'v'\rangle &= \left(E_{kc}^{QP}-E_{kv}^{QP}\right)\delta_{kk'}\delta_{cc'}\delta_{vv'} \\ &\quad -W_{k'c'v'}^{kcv}+\nu_{k'c'v'}^{kcv} \end{aligned} \tag{23}$$

Here v/c represents the index of the hole and electron. E_{kc}^{QP} and E_{kv}^{QP} are the quasi particle energies for the electron and hole respectively. $|kcv\rangle$ are the electron-hole-pair basis sets based on spinor formalism, which is constructed through the spin-orbit interaction. W and v represent the screened Coulomb and exchange interaction between the electron and hole. Using the BSE Hamiltonian of Eq.(21), the time-dependent two-particle Schrödinger equation can be solved and the CPA approximation is used following the TDKS-NAMD method. Combined with the expansion of the exciton state, the time propagation of the expansion coefficients can be written as,

$$\begin{aligned}i\hbar\dot{A}_{kcv} = \sum_{k'}\sum_{c'}^{\text{elec}}\sum_{v'}^{\text{hole}}\Big(&\langle kcv|H|k'c'v'\rangle \\ &-i\hbar\langle kcv|\frac{\partial}{\partial t}|k'c'v'\rangle\Big)A_{k'c'v'}\end{aligned} \tag{24}$$

Coherent time evolution of excitonic states coupled to the nuclear subsystem is described in Eq.(24).

The most challenging part for the application of GW+rtBSE-NAMD method is the GW calculation for each time step. For example, for a simulation of a ps timescale trajectory, 10^3 times of GW calculation is needed, the ultra-expensive computational cost makes the simulation to be difficult. To overcome such difficulty, the rigid dielectric function approximation is proposed where the dielectric function which is required to calculate W is assumed not to change during the *ab initio* MD simulation. This approximation is reasonable if the temperature is far away from the phase transition point. Based on this approximation, only a single point G_0W_0 is needed to achieve the dielectric function. The quasi particle energies can be calculated using the scissor operator by adding $\Delta E_{GW\text{-PBE}}$ to the PBE KS energies.

Using the GW+rtBSE-NAMD method, a comprehensive picture of spin-valley exciton dynamics for the monolayer MoS_2 is obtained [47], where the electron-phonon, spin-orbital coupling and electron-hole many body effects come into playing collectively as schemat-

DOI:10.1063/1674-0068/cjcp2111233 ©2022 Chinese Physical Society

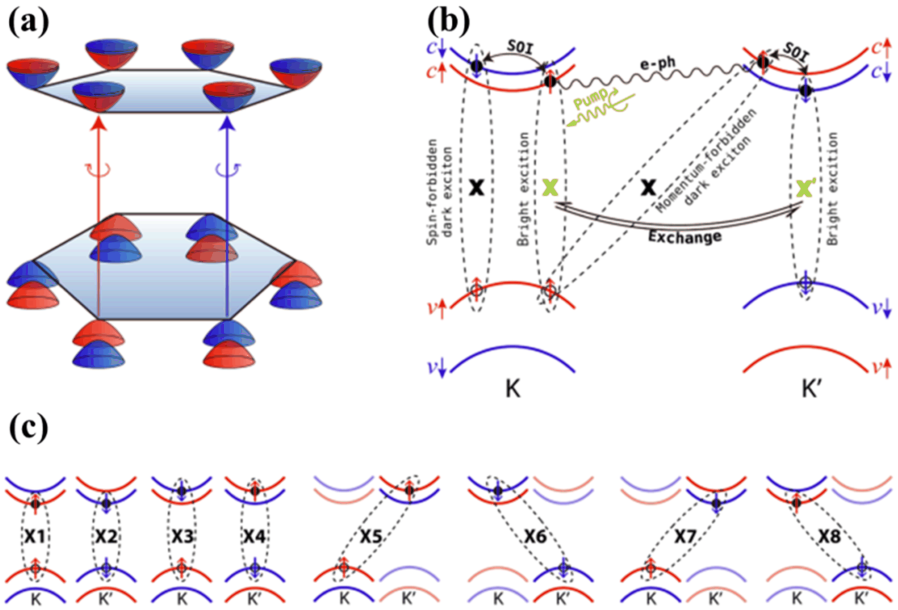

FIG. 7 Schematic spin-valley dynamics in MoS_2 systems. (a) The band structure at the band edges near K and K'. (b) The intervalley bright exciton transition and bright-to-dark exciton transition processes. They are induced by electron-hole exchange, spin-orbit interaction, and electron-phonon coupling, respectively. (c) The electron-hole pairs involved during the exciton dynamics. Adapted with permission from Ref.[47]. Copyright 2021 American Association for the Advancement of Science.

ically shown in FIG. 7. It is found that the fast bright valley exciton scattering is due to the electron-hole exchange interaction, which is in good agreement with experiments, while the spin-orbital coupling and electron-phonon coupling are responsible for the bright-to-dark exciton transition.

D. Chemical reactions and growth

Reactions in the growth of nanosystems are important topics of nanosciences. For example, it is essential to understand the underlying growth mechanisms for mass production of high-quality graphene samples. Under the growth conditions, it is not practical to obtain atomic details in experiment, which calls for computational characterization of such processes. To directly compare with macroscopic observation in experiment, multiscale simulation techniques should be developed.

In principle, MD provides a direct way to simulate the dynamic process of the growth. However, its accessible time scale is much shorter than that of graphene growth, which makes MD more suitable for studying specific problems instead of obtaining an overall picture. As a time scale coarse grain technique, kMC can be used to study growth dynamics [50, 51, 52, 56]. In kMC simulations, kinetic parameters for elementary reactions should be provided. Reaction rate of an elementary reaction can be usually estimated by harmonic transition state theory after the energy barrier is obtained from first principles. If the system is significantly anharmonic, for example a metal surface at a temperature closing to the melting point of the metal, explicitly sampling all configurations may be required.

Sampling typically should be performed with an enhanced sampling technique, such as metadynamics [143]. In metadynamics, a history-dependent bias potential is applied in a MD simulation to escape from local minima in the free energy surface.

$$V_{\text{meta}} = \sum_{t'=\delta t,2\delta t\ldots}^{t<t''} W \prod_{i=1}^{N_{CV}} \exp\left[-\frac{\left(\xi_i - \xi_i\left(t'\right)\right)^2}{2\delta\xi_i^2}\right] \quad (25)$$

where ξ_i is one of the N_{CV} collective variables, W and $\delta\xi_i$ are height and width of the Gaussian. δt is the period of the Gaussian potential added. Finally, the potential of mean force can be obtained from the added potential.

$$\lim_{t\to\infty} V_{\text{meta}}\left(t\right) = -F \quad (26)$$

First principles sampling is computationally very ex-

DOI:10.1063/1674-0068/cjcp2111233 ©2022 Chinese Physical Society

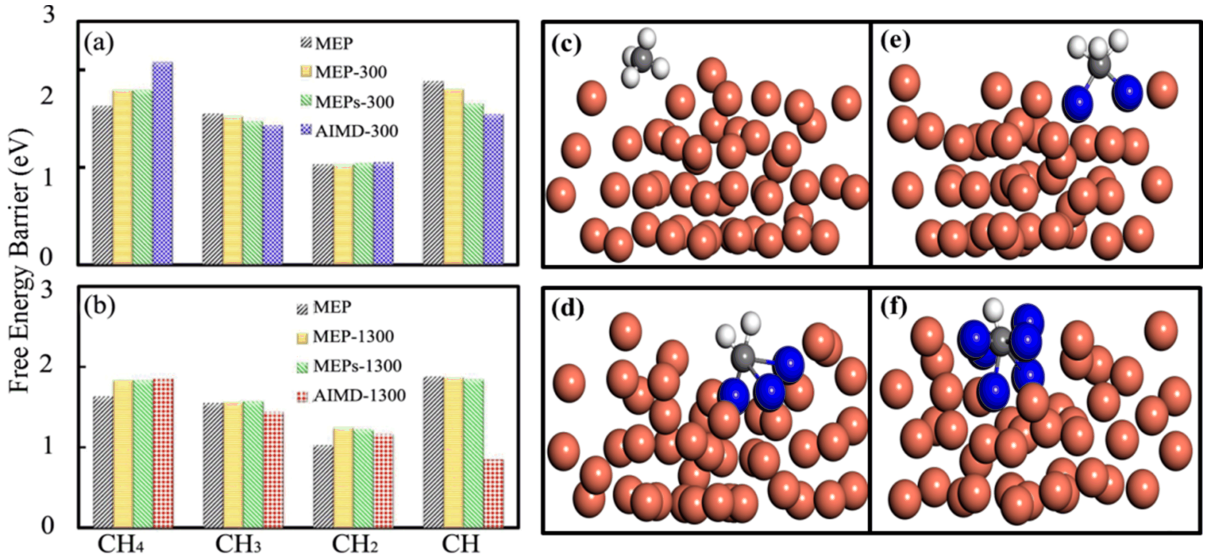

FIG. 8 Activation energy (black) and free-energy barrier (yellow, green, red, and blue) of CH_4, CH_3, CH_2, and CH dehydrogenation at (a) 300 K and (b) 1300 K. A typical reactant-state snapshot of the *ab initio* MD trajectory for (c) CH_4, (e) CH_3, (d) CH_2, and (f) CH dehydrogenation at 1300 K. Adapted from Ref.[48]. Copyright 2021 Chinese Chemical Society.

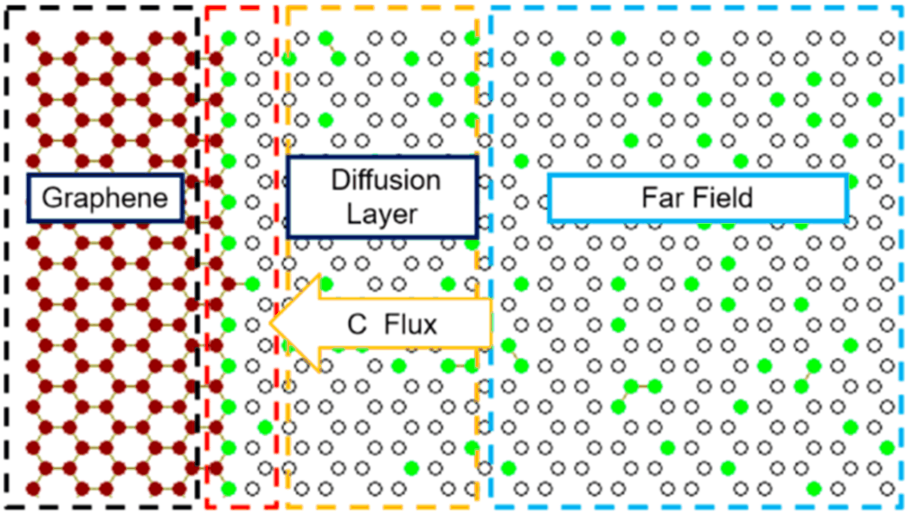

FIG. 9 Schematic diagram of the standing-on-the-growth-front kMC model. Solid and hollow circles represent occupied and unoccupied lattice sites. Brown sites have already formed graphene. For simplicity, surface sites for carbon adsorption are represented by a honeycomb lattice. Adapted from Ref.[52]. Copyright 2012 American Chemical Society.

pensive. Fortunately, it is not always necessary, even if the metal surface is melting. It is found that, if the local chemical environment can be maintained, high-temperature surface reactions can still effectively follow the minimum energy path [48]. In a comparison of MD sampling results and minimum energy path based results, it is found that the obtained free energy barrier for dehydrogenation reactions of CH_x on Cu (111) surface at 1300 K is similar except the x=1 case (FIG. 8). The reason is that the steric hindrance effect makes the local chemical environment of CH_3 and CH_2 on a melting surface still similar to that on a crystalline surface. Even if they are totally disordered, there is only a limited space available for Cu atoms to approach C. As a result, the coordination of Cu to C is similar to those species on crystal Cu(111) surface. For small species, such as CH, Cu atoms can warp the C atom around. The local chemical environment is thus significantly different from CH adsorbed on Cu(111) surface. Therefore, in order to obtain reaction rate constants for

DOI:10.1063/1674-0068/cjcp2111233 ©2022 Chinese Physical Society

this set of dehydrogenations at 1300 K, MD sampling is only required for CH dehydrogenation.

By checking the local chemical environment, we can save the computational cost for preparing kinetic parameters for high-temperature kMC simulations. However, sometime kMC simulations itself can be computationally very expensive. In kMC simulations, all possible events are listed in a table, and a specific event is selected with a probability proportional to its rate. When the rate of different events are very different, slow event can be hardly sampled, which makes the kMC simulation inefficient. In such a case, a timescale separation technique can be used [52] or alternatively a mean field approximation can be applied to a specific species, such as H adatom in graphene growth. With such techniques, dominant feeding species of graphene growth have been identified [51]. Another challenge for kMC simulation of growth is that, to obtain a statistically significant growth rate, the growth front must be propagated forward over a long distance, which requires a very large simulation cell. To solve this problem, a standing-on-the-growth-front model [52] has been developed to speed up kMC simulations. As shown in FIG. 9, the whole system of graphene growth is divided into four regions: graphene area, growth front, diffusion layer, and far field. If we focus on the growth front with carbon flux as a parameter which can be obtained from an equilibrium far field and the carbon diffusivity, we can use a very small box (red box in FIG. 9) to carry out kMC simulation very efficiently, which has been used to directly reproduce the experimental observed nonlinear growth behavior [52].

IV. CONCLUSION

In this review, we have presented various algorithms or softwares recently developed for characterizing nanosystems. Linear-scaling DFT method based on numerical atomic basis set can be used for large-scale system hybrid functional calculations, which has been implemented in the HONPAS software. A fast method under the framework of the Bardeen perturbation approximation with fast Fourier transform to simulate STM images has been proposed to efficiently study systems with complex STM tips. For characterizing of open quantum impurity systems, the HEOM-QUICK software has been developed, which combined with DFT calculations can capture a lot of features such as the system-environment dissipation, many-body interactions, and non-Markovian memory. *Ab initio* Hefei-NAMD code under the fewest switches surface hopping CPA framework is suitable for the calculation of excited carrier dynamics, which can provide deep insights in understanding ultrafast dynamics process in various systems. Multiscale simulation methods with various acceleration techniques have been proposed to simulate the complex graphene growth process. With these algorithms and softwares, an accurate and efficient characterization of large-scale nanosystems under practical conditions becomes feasible. Progresses in this direction will significantly deepen our understanding of the nanoworld.

V. ACKNOWLEDGMENTS

This work was supported by the Ministry of Science and Technology (No.2016YFA0200604).

[1] A. Szabo and N. S. Ostlund, *Modern Quantum Chemistry: Introduction to Advanced Electronic Structure Theory*, New York: Dover Publications, (1996).
[2] A. J. Cohen, P. Mori-Sánchez, and W. Yang, Chem. Rev. **112**, 289 (2012).
[3] A. D. Becke, J. Chem. Phys. **98**, 5648 (1993).
[4] J. Heyd, G. E. Scuseria, and M. Ernzerhof, J. Chem. Phys. **118**, 8207 (2003).
[5] J. Paier, M. Marsman, K. Hummer, G. Kresse, I. C. Gerber, and J. G. Angyán, J. Chem. Phys. **124**, 154709 (2006).
[6] A. D. Becke, J. Chem. Phys. **98**, 1372 (1993).
[7] J. P. Perdew, M. Ernzerhof, and K. Burke, J. Chem. Phys. **105**, 9982 (1996).
[8] S. Baroni, S. De Gironcoli, A. Dal Corso, and P. Giannozzi, Rev. Mod. Phys. **73**, 515 (2001).
[9] G. P. Lopinski, D. J. Moffatt, D. D. M. Wayner, and R. A. Wolkow, Nature **392**, 909 (1998).
[10] X. Qiu, C. Wang, Q. Zeng, B. Xu, S. Yin, H. Wang, S. Xu, and C. Bai, J. Am. Chem. Soc. **122**, 5550 (2000).
[11] A. Zhao, Q. Li, L. Chen, H. Xiang, W. Wang, S. Pan, B. Wang, X. Xiao, J. Yang, J. G. Hou, and Q. Zhu, Science **309**, 1542 (2005).
[12] R. Zhang, Y. Zhang, Z. C. Dong, S. Jiang, C. Zhang, L. G. Chen, L. Zhang, Y. Liao, J. Aizpurua, Y. Luo, J. L. Yang, and J. G. Hou, Nature **498**, 82 (2013).
[13] J. G. Hou, J. Yang, H. Wang, Q. Li, C. Zeng, H. Lin, W. Bing, D. M. Chen, and Q. Zhu, Phys. Rev. Lett. **83**, 3001 (1999).
[14] J. Tersoff and D. R. Hamann, Phys. Rev. Lett. **50**, 1998 (1983).

DOI:10.1063/1674-0068/cjcp2111233 ©2022 Chinese Physical Society

[15] J. Tersoff and D. R. Hamann, Phys. Rev. B **31**, 805 (1985).
[16] L. Bartels, G. Meyer, and K. H. Rieder, Appl. Phys. Lett. **71**, 213 (1997).
[17] J. R. Hahn, H. J. Lee, and W. Ho, Phys. Rev. Lett. **85**, 1914 (2000).
[18] C. Zeng, H. Wang, B. Wang, J. Yang, and J. G. Hou, Appl. Phys. Lett. **77**, 3595 (2000).
[19] L. Chen, Z. Hu, A. Zhao, B. Wang, Y. Luo, J. Yang, and J. G. Hou, Phys. Rev. Lett. **99**, 146803 (2007).
[20] J. Bardeen, Phys. Rev. Lett. **6**, 57 (1961).
[21] J. Park, A. N. Pasupathy, J. I. Goldsmith, C. Chang, Y. Yalsh, J. R. Petta, M. Rinkoski, J. P. Sethna, H. D. Abruña, P. L. McEuen, and D. C. Ralph, Nature **417**, 722 (2002).
[22] L. Z. Ye, X. Wang, D. Hou, R. X. Xu, X. Zheng, and Y. J. Yan, Wiley Interdiscip. Rev. Comput. Mol. Sci. **6**, 608 (2016).
[23] K. G. Wilson, Rev. Mod. Phys. **47**, 773 (1975).
[24] S. R. White, Phys. Rev. Lett. **69**, 2863 (1992).
[25] M. Caffarel and W. Krauth, Phys. Rev. Lett. **72**, 1545 (1994).
[26] J. E. Hirsch and R. M. Fye, Phys. Rev. Lett. **56**, 2521 (1986).
[27] S. Weiss, J. Eckel, M. Thorwart, and R. Egger, Phys. Rev. B **77**, 195316 (2008).
[28] H. D. Meyer, U. Manthe, and L. S. Cederbaum, Chem. Phys. Lett. **165**, 73 (1990).
[29] J. Jin, X. Zheng, and Y. Yan, J. Chem. Phys. **128**, 234703 (2008).
[30] Z. Li, N. Tong, X. Zheng, D. Hou, J. Wei, J. Hu, and Y. Yan, Phys. Rev. Lett. **109**, 266403 (2012).
[31] L. Cui, H. D. Zhang, X. Zheng, R. X. Xu, and Y. Yan, J. Chem. Phys. **151**, 024110 (2019).
[32] H. D. Zhang, L. Cui, H. Gong, R. X. Xu, X. Zheng, and Y. J. Yan, J. Chem. Phys. **152**, 064107 (2020).
[33] Y. Tanimura and R. Kubo, J. Phys. Soc. Jpn. **58**, 101 (1989).
[34] L. Han, H. D. Zhang, X. Zheng, and Y. Yan, J. Chem. Phys. **148**, 234108 (2018).
[35] M. Pavanello, D. J. Auerbach, A. M. Wodtke, M. Blanco-Rey, M. Alducin, and G. J. Kroes, J. Phys. Chem. Lett. **4**, 3735 (2013).
[36] A. M. Wodtke, Chem. Soc. Rev. **45**, 3641 (2016).
[37] J. Deslippe, G. Samsonidze, D. A. Strubbe, M. Jain, M. L. Cohen, and S. G. Louie, Comput. Phys. Commun. **183**, 1269 (2012).
[38] G. Onida, L. Reining, and A. Rubio, Rev. Mod. Phys. **74**, 601 (2002).
[39] Q. Zheng, W. Chu, C. Zhao, L. Zhang, H. Guo, Y. Wang, X. Jiang, and J. Zhao, Wiley Interdiscip. Rev. Comput. Mol. Sci. **9**, e1411 (2019).
[40] A. V. Akimov and O. V. Prezhdo, J. Chem. Theory Comput. **9**, 4959 (2013).
[41] S. Meng and E. Kaxiras, J. Chem. Phys. **129**, 054110 (2008).
[42] W. Li, L. Zhou, O. V. Prezhdo, and A. V. Akimov, ACS Energy Lett. **3**, 2159 (2018).
[43] G. Cui and W. Thiel, J. Chem. Phys. **141**, 124101 (2014).
[44] L. Wang, A. Akimov, and O. V. Prezhdo, J. Phys. Chem. Lett. **7**, 2100 (2016).
[45] J. C. Tully, J. Chem. Phys. **93**, 1061 (1990).
[46] R. Long, O. V. Prezhdo, and W. Fang, Wiley Interdiscip. Rev. Comput. Mol. Sci. **7**, e1305 (2017).
[47] X. Jiang, Q. Zheng, Z. Lan, W. A. Saidi, X. Ren, and J. Zhao, Sci. Adv. **7**, eabf3759 (2021).
[48] X. Zeng, Z. Qiu, P. Li, Z. Li, and J. Yang, CCS Chem. **2**, 460 (2020).
[49] Z. Qiu, L. Song, J. Zhao, Z. Li, and J. Yang, Angew. Chem. Int. Ed. **55**, 9918 (2016).
[50] P. Wu, Y. Zhang, P. Cui, Z. Li, J. Yang, and Z. Zhang, Phys. Rev. Lett. **114**, 216102 (2015).
[51] P. Li, Z. Li, and J. Yang, J. Phys. Chem. C **121**, 25949 (2017).
[52] P. Wu, H. Jiang, W. Zhang, Z. Li, Z. Hou, and J. Yang, J. Am. Chem. Soc. **134**, 6045 (2012).
[53] L. Wang, X. Zhang, H. L. W. Chan, F. Yan, and F. Ding, J. Am. Chem. Soc. **135**, 4476 (2013).
[54] E. Meca, J. Lowengrub, H. Kim, C. Mattevi, and V. B. Shenoy, Nano Lett. **13**, 5692 (2013).
[55] G. Li, S. H. Huang, and Z. Li, Phys. Chem. Chem. Phys. **17**, 22832 (2015).
[56] P. Li and Z. Li, J. Phys. Chem. C **124**, 16233 (2020).
[57] Z. Qiu, P. Li, and Z. Li, J. Yang, Acc. Chem. Res. **51**, 728 (2018)
[58] P. Li and Z. Li, Sci. Bull. **63**, 3419 (2018).
[59] P. Wu, W. Zhang, Z. Li, and J. Yang, Small **10**, 2136 (2014).
[60] R. G. Parr and W. Yang, *Density-Functional Theory of Atoms and Molecules*, New York: Oxford University Press, (1989).
[61] S. Goedecker, Rev. Mod. Phys. **71**, 1085 (1999).
[62] D. R. Bowler and T. Miyazaki, Rep. Prog. Phys. **75**, 036503 (2012).
[63] W. Kohn, Int. J. Quantum Chem. **56**, 229 (1995).
[64] J. M. Soler, E. Artacho, J. D. Gale, A. Garca, J. Junquera, P. Ordejón, and D. Sánchez-Portal, J. Phys.: Condens. Matter **14**, 2745 (2002).
[65] B. Delley, J. Chem. Phys. **92**, 508 (1990).
[66] T. Ozaki, Phys. Rev. B **67**, 155108 (2003).
[67] X. Qin, H. Shang, H. Xiang, Z. Li, and J. Yang, Int. J. Quantum Chem. **115**, 647 (2015).
[68] W. Yang, Phys. Rev. Lett. **66**, 1438 (1991).
[69] X. P. Li, R. W. Nunes, and D. Vanderbilt, Phys. Rev. B **47**, 10891 (1993).

DOI:10.1063/1674-0068/cjcp2111233 ©2022 Chinese Physical Society

[70] A. M. N. Niklasson, Phys. Rev. B **66**, 155115 (2002).
[71] A. M. N. Niklasson, C. J. Tymczak, and M. Challacombe, J. Chem. Phys. **118**, 8611 (2003).
[72] A. M. N. Niklasson, C. J. Tymczak, and H. Röder, Phys. Rev. B **66**, 155120 (2002).
[73] H. J. Xiang, W. Z. Liang, J. Yang, J. G. Hou, and Q. Zhu, J. Chem. Phys. **123**, 124105 (2005).
[74] H. J. Xiang, J. Yang, J. G. Hou, and Q. Zhu, J. Chem. Phys. **126**, 244707 (2007).
[75] H. J. Xiang, Z. Li, W. Z. Liang, J. Yang, J. G. Hou, and Q. Zhu, J. Chem. Phys. **124**, 234108 (2006).
[76] H. J. Xiang, J. Yang, J. G. Hou, and Q. Zhu, Phys. Rev. Lett. **97**, 266402 (2006).
[77] D. M. Ceperley and B. J. Alder, Phys. Rev. Lett. **45**, 566 (1980).
[78] J. P. Perdew, K. Burke, and M. Ernzerhof, Phys. Rev. Lett. **77**, 3865 (1996).
[79] P. Mori-Sánchez, A. J. Cohen, and W. Yang, Phys. Rev. Lett. **100**, 146401 (2008).
[80] H. Shang, Z. Li, and J. Yang, J. Phys. Chem. A **114**, 1039 (2010).
[81] E. Schwegler, M. Challacombe, and M. Head-Gordon, J. Chem. Phys. **106**, 9708 (1997).
[82] A. F. Izmaylov, G. E. Scuseria, and M. J. Frisch, J. Chem. Phys. **125**, 104103 (2006).
[83] D. S. Lambrecht and C. Ochsenfeld, J. Chem. Phys. **123**, 184101 (2005).
[84] H. Shang, Z. Li, and J. Yang, J. Chem. Phys. **135**, 034110 (2011).
[85] H. Shang, L. Xu, B. Wu, X. Qin, Y. Zhang, and J. Yang, Comput. Phys. Commun. **254**, 107204 (2020).
[86] X. Qin, H. Shang, L. Xu, W. Hu, J. Yang, S. Li, and Y. Zhang, Int. J. High Perform. Comput. Appl. **34**, 159 (2020).
[87] J. L. Whitten, J. Chem. Phys. **58**, 4496 (1973).
[88] F. Weigend, Phys. Chem. Chem. Phys. **4**, 4285 (2002).
[89] W. Hu, L. Lin, A. S. Banerjee, E. Vecharynski, and C. Yang, J. Chem. Theory Comput. **13**, 1188 (2017).
[90] J. Lu and L. Ying, J. Comput. Phys. **302**, 329 (2015).
[91] X. Qin, J. Liu, W. Hu, and J. Yang, J. Phys. Chem. A **124**, 5664 (2020).
[92] W. Hu, L. Lin, and C. Yang, J. Chem. Theory Comput. **13**, 5420 (2017).
[93] K. Dong, W. Hu, and L. Lin, J. Chem. Theory Comput. **14**, 1311 (2018).
[94] X. Qin, J. Li, W. Hu, and J. Yang, J. Phys. Chem. A **124**, 10066 (2020).
[95] W. Hu, J. Liu, Y. Li, Z. Ding, C. Yang, and J. Yang, J. Chem. Theory Comput. **16**, 964 (2020).
[96] H. Ma, L. Wang, L. Wan, J. Li, X. Qin, J. Liu, W. Hu, L. Lin, C. Yang, and J. Yang, J. Phys. Chem. A **125**, 7545 (2021).
[97] G. Binnig, H. Rohrer, C. Gerber, and E. Weibel, Appl. Phys. Lett. **40**, 178 (1982).
[98] G. Binnig, H. Rohrer, C. Gerber, and E. Weibel, Phys. Rev. Lett. **50**, 120 (1983).
[99] G. Binnig and H. Rohrer, Surf. Sci. **126**, 236 (1983).
[100] T. Fujita, H. Nakai, and H. Nakatsuji, J. Chem. Phys. **104**, 2410 (1996).
[101] G. A. D. Briggs and A. J. Fisher, Surf. Sci. Rep. **33**, 1 (1999).
[102] M. B̈-ttiker, Y. Imry, R. Landauer, and S. Pinhas, Phys. Rev. B **31**, 6207 (1985).
[103] W. A. Hofer, A. S. Foster, and A. L. Shluger, Rev. Mod. Phys. **75**, 1287 (2003).
[104] H. Ness and A. Fisher, Phys. Rev. B **56**, 12469 (1997).
[105] H. Ren, J. Yang, and Y. Luo, J. Chem. Phys. **133**, 064702 (2010).
[106] B. C. Stipe, M. A. Rezaei, and W. Ho, Science **279**, 1907(1998).
[107] H. Wang, C. Zeng, Q. Li, B. Wang, J. Yang, J. G. Hou, and Q. Zhu, Surf. Sci. **442**, L1024 (1999).
[108] A. M. Ferrari, C. Pisani, F. Cinquini, L. Giordano, and G. Pacchioni, J. Chem. Phys. **127**, 174711 (2007).
[109] L. Zhao, M. Levendorf, S. Goncher, T. Schiros, L. Palova, A. Zabet-Khosousi, K. T. Rim, C. Gutierrez, D. Nordlund, C. Jaye, M. Hybertsen, D. Reichman, G. W. Flynn, J. Park, and A. N. Pasupathy, Nano Lett. **13**, 4659 (2013).
[110] Y. Chen, T. Cao, C. Chen, Z. Pedramrazi, D. Haberer, D. G. de Oteyza, F. R. Fischer, S. G. Louie, and M. F. Crommie, Nat. Nanotechnol. **10**, 156 (2015).
[111] Ó. Paz, I. Brihuega, J. M. Gómez-Rodríguez, and J. M. Soler, Phys. Rev. Lett. **94**, 056103 (2005).
[112] R. Zhang, Z. Hu, B. Li, and J. Yang, J. Phys. Chem. A **118**, 8953 (2014).
[113] S. Wang, X. Zheng, J. Jin, and Y. Yan, Phys. Rev. B **88**, 035129 (2013).
[114] X. Zheng, R. Xu, J. Xu, J. Jin, J. Hu, and Y. Yan, Prog. Chem. **24**, 1129 (2012).
[115] X. Zheng, J. Jin, and Y. Yan, J. Chem. Phys. **129**, 184112 (2008).
[116] X. Zheng, J. Jin, S. Welack, M. Luo, and Y. Yan, J. Chem. Phys. **130**, 164708 (2009).
[117] P. W. Anderson, Phys. Rev. **124**, 41 (1961).
[118] D. Hou, R. Wang, X. Zheng, N. Tong, J. Wei, and Y. Yan, Phys. Rev. B **90**, 045141 (2014).
[119] Y. Tanimura and P. G. Wolynes, Phys. Rev. A **43**, 4131 (1991).
[120] Y. Tanimura and P. G. Wolynes, J. Chem. Phys. **96**, 8485 (1992).
[121] J. Hu, R. X. Xu, and Y. Yan, J. Chem. Phys. **133**, 101106 (2010).
[122] J. Hu, M. Luo, F. Jiang, R. X. Xu, and Y. Yan, J. Chem. Phys. **134**, 244106 (2011).
[123] L. Ye, H. D. Zhang, Y. Wang, X. Zheng, and Y. Yan,

DOI:10.1063/1674-0068/cjcp2111233 ©2022 Chinese Physical Society

J. Chem. Phys. **147**, 074111 (2017).
[124] D. Hou, S. Wang, R. Wang, L. Ye, R. Xu, X. Zheng, and Y. Yan, J. Chem. Phys. **142**, 104112 (2015).
[125] X. Wang, D. Hou, X. Zheng, and Y. Yan, J. Chem. Phys. **144**, 034101 (2016).
[126] Y. Wang, X. Zheng, and J. Yang, Phys. Rev. B **93**, 125114 (2016).
[127] Y. Wang, X. Zheng, B. Li, and J. Yang, J. Chem. Phys. **141**, 084713 (2014).
[128] X. Li, L. Zhu, B. Li, J. Li, P. Gao, L. Yang, A. Zhao, Y. Luo, J. Hou, X. Zheng, B. Wang, and J. Yang, Nat. Commun. **11**, 2566 (2020).
[129] M. Bernardi, M. Palummo, and J. C. Grossman, Nano Lett. **13**, 3664 (2013).
[130] A. Fujishima and K. Honda, Nature **238**, 37 (1972).
[131] C. J. Docherty, P. Parkinson, H. J. Joyce, M. H. Chiu, C. H. Chen, M. Y. Lee, L. J. Li, L. M. Herz, and M. B. Johnston, ACS Nano **8**, 11147 (2014).
[132] T. Korn, S. Heydrich, M. Hirmer, J. Schmutzler, and C. Schller, Appl. Phys. Lett. **99**, 102109 (2011).
[133] S. L. Fiedler and J. Eloranta, Mol. Phys. **108**, 1471 (2010).
[134] J. C. Tully, J. Chem. Phys. **137**, 22A301 (2012).
[135] E. Runge and E. K. U. Gross, Phys. Rev. Lett. **52**, 997 (1984).
[136] Q. Zheng, W. A. Saidi, Y. Xie, Z. Lan, O. V. Prezhdo, H. Petek, and J. Zhao, Nano Lett. **17**, 6435 (2017).
[137] Q. Zheng, Y. Xie, Z. Lan, O. V. Prezhdo, W. A. Saidi, and J. Zhao, Phys. Rev. B **97**, 205417 (2018).
[138] W. Chu, W. A. Saidi, Q. Zheng, Y. Xie, Z. Lan, O. V. Prezhdo, H. Petek, and J. Zhao, J. Am. Chem. Soc. **138**, 13740 (2016).
[139] W. Chu, Q. Zheng, O. V. Prezhdo, J. Zhao, and W. A. Saidi, Sci. Adv. **6**, eaaw7453 (2020).
[140] L. Zhang, W. Chu, Q. Zheng, A. V. Benderskii, O. V. Prezhdo, and J. Zhao, J. Phys. Chem. Lett. **10**, 6151 (2019).
[141] L. Zhang, Q. Zheng, Y. Xie, Z. Lan, O. V. Prezhdo, W. A. Saidi, and J. Zhao, Nano Lett. **18**, 1592 (2018).
[142] C. Zhao, Q. Zheng, J. Wu, and J. Zhao, Phys. Rev. B **96**, 134308 (2017).
[143] A. Laio and M. Parrinello, Proc. Natl. Acad. Sci. USA **99**, 12562 (2002).

DOI:10.1063/1674-0068/cjcp2111233 ©2022 Chinese Physical Society